Supporting Information for "Creep Rheology of Antigorite: Experiments at Subduction Zone Conditions"

Eric Burdette and Greg Hirth

[1]Department of Earth, Environmental and Planetary Sciences, Brown University, Providence, RI, USA

Contents

Introduction

Here we have included supporting details describing microstructure, calibration, more extensive comparison of our results to other work, and detailed methods used to collect and process strain rate data. In addition we have included the rheological data points and details about the fitting methodology used.

Text S1. Mechanical Data Calculations

The Griggs apparatus has both external load and displacement sensors which need to be corrected to find load and displacement on the sample inside the pressure vessel. Differential stress is determined by subtracting a "hit point" stress (hydrostatic pressure+friction) from the externally measured load. Displacement is determined by subtracting displacement absorbed by the column in compression (Burdette & Hirth, 2020), and referenced relative to the "hit point".

$$x_{sample} = x_{LVDT2} - \frac{\sigma_{1,external}}{k_{lower\_column}} \tag{1}$$

To calculate permanent/inelastic strain, elastic compression of the sample can also be removed:

$$k_{sample} = \frac{E}{l_{sample}} \tag{2}$$

$$x_{inelastic} = x_{LVDT2} - \frac{\sigma_{1,external}}{k_{lower\_column}} - \frac{\sigma_{differential,internal}}{k_{sample}} \tag{3}$$

Note that these equations assume sample elasticity is constant, and don't account for rate-dependent friction.

To calculate strain rates during post-processing, we used the first derivative of a first order Savitzky-Golay filter (moving line fit) over a moving time window chosen for each step. For strain rates above $10^{-6}1/s$, the window could be as short as 100 seconds, while the lowest strain rates require a 10000 second time window. Strain rates chosen for flow law fits were the final point that was not influenced by a disturbance or loading to the next stress. Wherever strain rate is plotted as a continuous function of time (e.g. Figures 3-5), a single window length was chosen over the whole plot to best display data. Data from a slow strain rate step is displayed in Figure S1.

Corresponding author: Eric Burdette, `eric_burdette@brown.edu`

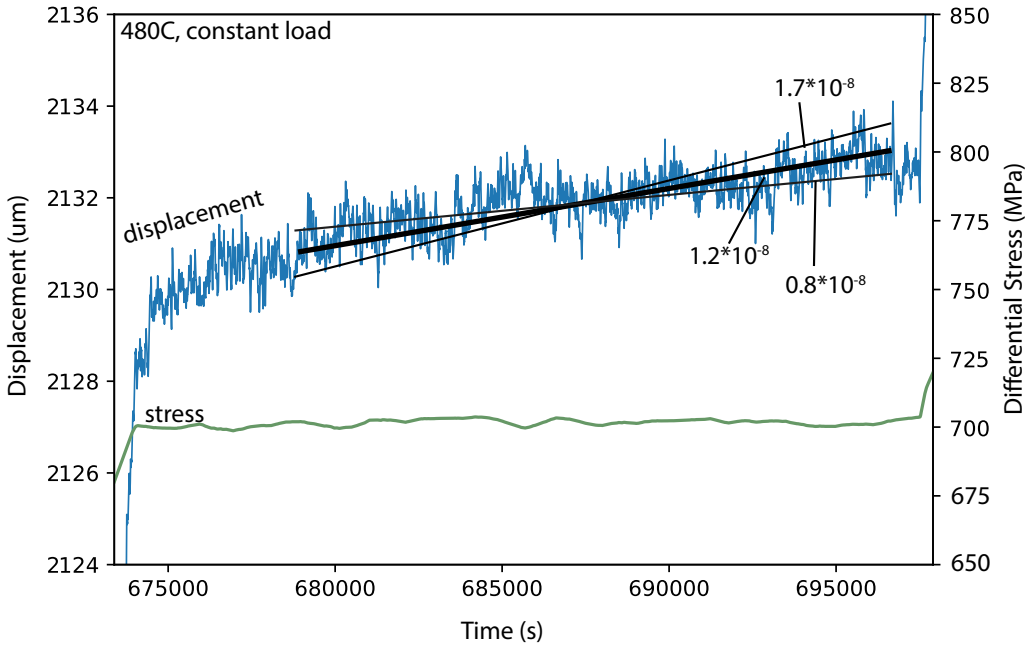

Figure S1. Load and Displacement plotted against time to show strain rate evolution during a stress step. For "low" stresses, the displacement resolution limits determination of strain rate

Text S2. Comparison of Mechanical Data to Other Works

Generally, samples deformed at 1 GPa have very similar strength to our samples as noted in the text.

The samples tested in Hilairet et al. (2007) are weaker (50%) than most other published results. The weakness could a result of to several factors, the most notable is the high degree of comminution due to damage during pressurization and repeated compression-tension deformation (Amiguet et al., 2014, Figure 6). In addition, the exponential law recommended after a companion microstructure study (Amiguet et al., 2014) does not extrapolate to low strain rates. Although the dislocation creep fit to data extrapolates reasonably, there is no evidence for dislocation climb or recrystallization in microstructural studies (Amiguet et al., 2014) that would justify its extrapolation.

Text S3. Hardening During Stress Steps

During individual stress steps samples harden over time (Figure 3). Hardening is expected to some extent from other descriptions/results of brittle creep and high temperature creep tests where primary, secondary, and tertiary creep phases can be identified. For westerly granite calibration tests (Figure 2), at each step samples reach constant strain rates after relatively small strains (0.2%). Post-processing of antigorite data shows that it may continue to harden after similar 0.2% strain steps (Figure 3).

Text S4. Flow Law Fit Methodology

A low temperature plasticity flow law was fit to stress vs. log(strainrate) using a Markov-chain Monte-Carlo (MCMC-NUTS via PyMC3) optimizer due to the small lo-

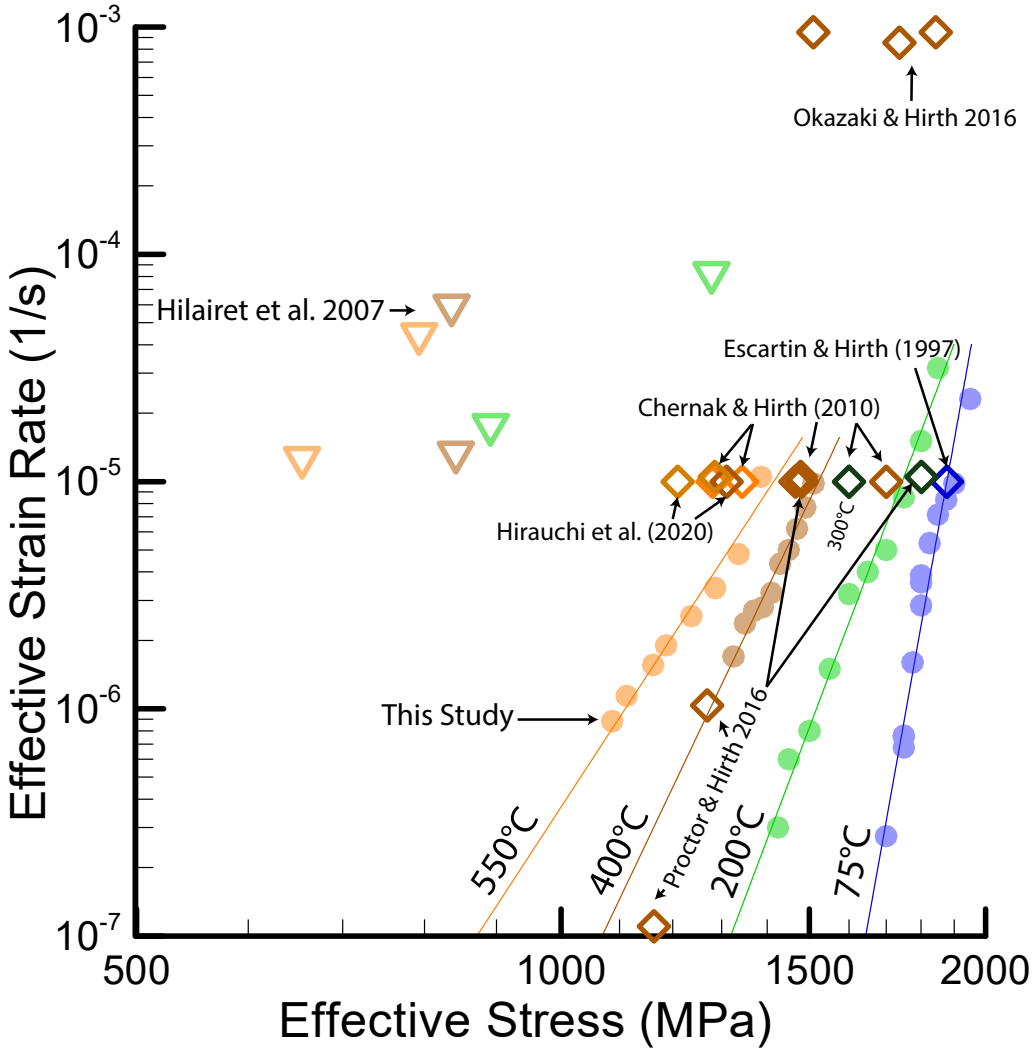

Figure S2. Compilation of other high pressure experimental antigorite deformation results plotted over results from the current study. Colors of points denotes temperature for all points. Both cores (Hirauchi et al., 2020; Chernak & Hirth, 2010; Escartin et al., 1997) and gouge (Chernak & Hirth, 2010; Proctor & Hirth, 2016; Okazaki & Hirth, 2016) are plotted.

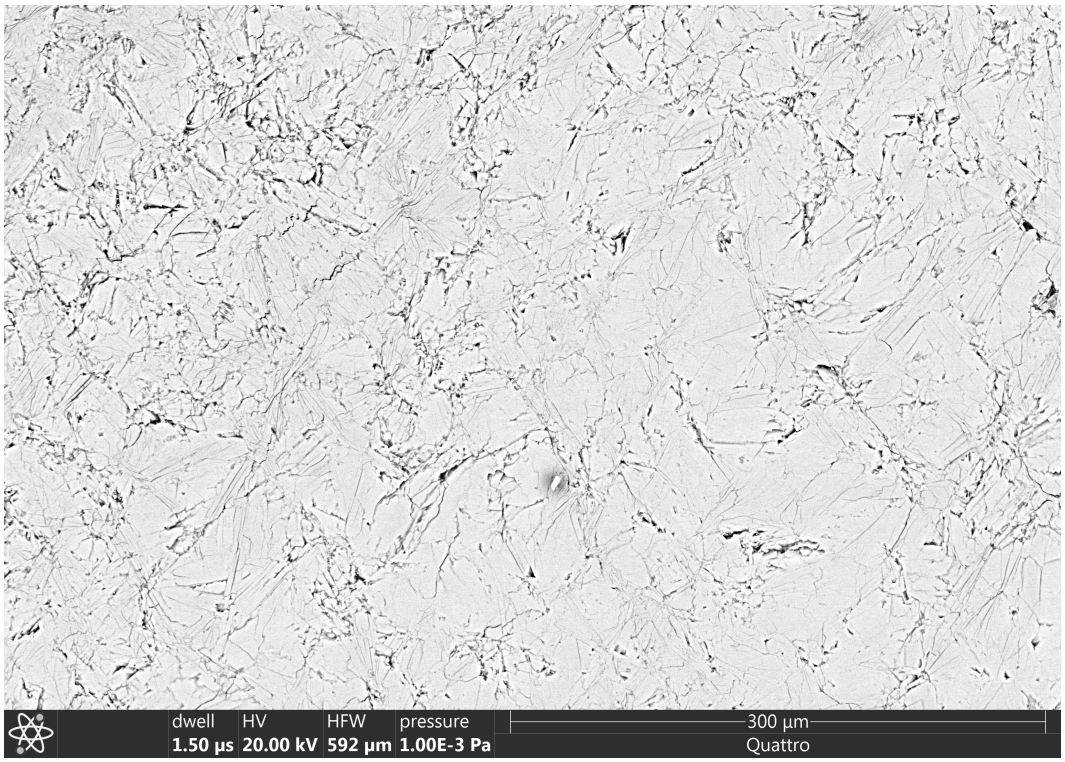

Figure S3. SEM image of intermediate zoom and multiple intersections at 200C. Voids are present due to grain pull-out during polishing. The featured intersection is near the top left corner.

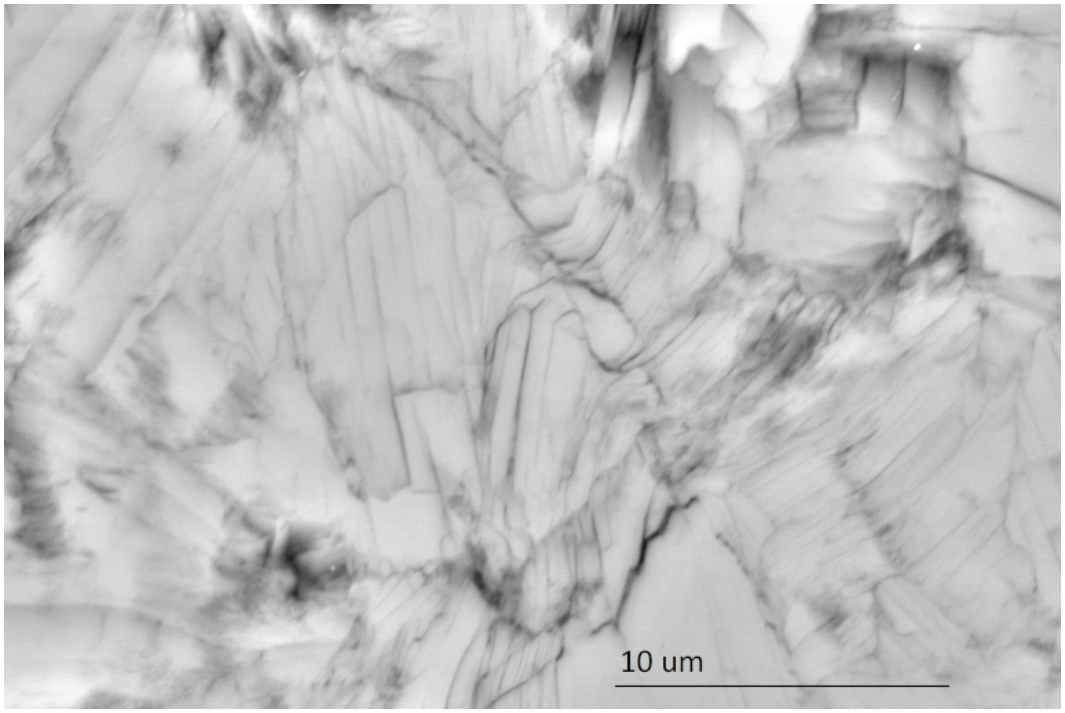

Figure S4. Gentle curvature of sheets recovered from 550°C sample.

cal discontinuities in the fit. Stress and strain error were included in the fit with input distributions of ±40 MPa and $3 - 1.5x$ 1/s centered around each point. Results with errors are presented in Table 2 and distributions of the posterior are plotted in Figure S5. 400000 samples were taken across 50 chains after burn-in to ensure accuracy of the fit. The upper and lower highest density intervals are included in addition to the standard deviation intervals because they contain information about the skewness of the distribution if it is not exactly Gaussian.

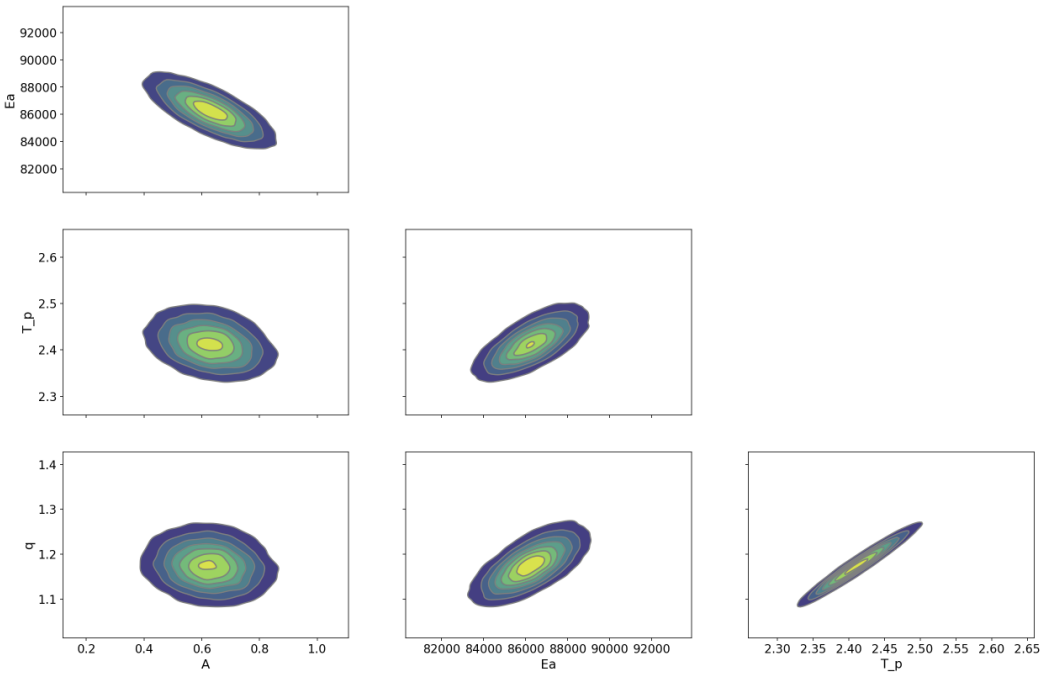

Figure S5. Posterior probability density functions in parameter space for the MCMC fit.

Low stress data have a larger influence on the extrapolated fit because they define the transition between defect density and temperature activation dominated regions of the low temperature plasticity flow law. The start of this transition can be seen in the slight curvature of the fit around points at 480°C in Figure 5b. In the LTP flow law, the region is defined by exponents p, q, and normalization factor τ_p. Below the transition at low stresses, the external term with σ^2 (proportional to defect density) dominates stress dependence.

Table 1: Creep data

Initial Strainrate (1/s)	Final Strainrate (1/s)	Initial Strain	Final Strain	Stress (MPa)	T (°C)	Experiment
6.80E-06	3.60E-06	0.0064	0.01	1800	75	W2441
9.40E-06	5.36E-06	0.01	0.016	1825	75	W2441
1.30E-05	7.15E-06	0.016	0.024	1850	75	W2441
1.42E-05	8.30E-06	0.024	0.034	1875	75	W2441
1.60E-05	9.80E-06	0.034	0.05	1900	75	W2441
3.00E-05	2.31E-05	0.05	0.07	1950	75	W2441
8.00E-07	3.00E-07	0.00042	0.00087	1425	200	W2447
1.00E-06	6.00E-07	0.00087	0.0011	1450	200	W2447

Continuation of Table 1						
1.00E-06	8.00E-07	0.0011	0.00178	1500	200	W2447
2.20E-06	1.50E-06	0.00178	0.00268	1550	200	W2447
5.00E-06	3.20E-06	0.00268	0.00338	1600	200	W2447
7.00E-06	4.00E-06	0.00338	0.00423	1650	200	W2447
1.10E-05	5.00E-06	0.00423	0.00559	1700	200	W2447
1.30E-05	8.51E-06	0.00559	0.0071	1750	200	W2447
2.60E-05	1.51E-05	0.0071	0.0096	1800	200	W2447
5.20E-05	3.16E-05	0.0096	0.0148	1850	200	W2447
2.25E-06	1.70E-06	0.0055	0.007	1325	400	W2439
2.80E-06	2.38E-06	0.007	0.009	1350	400	W2439
3.40E-06	2.70E-06	0.009	0.011	1370	400	W2439
3.80E-06	2.80E-06	0.011	0.0133	1390	400	W2439
4.00E-06	3.24E-06	0.0133	0.016	1410	400	W2439
5.00E-06	4.35E-06	0.016	0.019	1430	400	W2439
6.90E-06	5.00E-06	0.019	0.023	1450	400	W2439
7.80E-06	6.20E-06	0.023	0.028	1470	400	W2439
9.40E-06	7.70E-06	0.028	0.0325	1490	400	W2439
1.05E-05	9.80E-06	0.0325	0.036	1510	400	W2439
1.40E-06	8.82E-07	0.0005	0.00138	1062	550	W2424
1.60E-06	1.14E-06	0.00138	0.0024	1088	550	W2424
3.00E-06	1.56E-06	0.0024	0.00373	1137	550	W2424
2.60E-06	1.90E-06	0.00373	0.00474	1162	550	W2424
5.40E-06	2.56E-06	0.00474	0.00705	1212	550	W2424
7.50E-06	3.40E-06	0.00705	0.0106	1261	550	W2424
9.00E-06	4.80E-06	0.0106	0.015	1311	550	W2424
1.40E-05	1.05E-05	0.015	0.023	1361	550	W2424
8.00E-09	5.00E-09	0.0001	0.001	480	520	W2520
2.20E-08	1.70E-08	0.001	0.0022	600	520	W2520
4.00E-08	3.40E-08	0.0022	0.0033	690	520	W2520
8.00E-08	6.00E-08	0.0033	0.0048	790	520	W2520
9.50E-08	7.50E-08	0.0048	0.0063	880	520	W2520
5.00E-09	4.50E-09	0.0063	0.0067	470	520	W2520
1.40E-07	1.20E-07	0.0067	0.018	970	520	W2520
1.41E-09	1.40E-09	0.0001	0.0003	1230	76	W2521
4.00E-09	2.50E-09	0.0003	0.0005	1280	76	W2521
8.00E-08	5.00E-09	0.0005	0.0008	1330	76	W2521
2.50E-08	1.50E-08	0.0008	0.0015	1380	76	W2521
5.00E-08	3.00E-08	0.0015	0.0028	1430	76	W2521
2.50E-07	6.00E-08	0.0028	0.0046	1480	76	W2521
1.60E-06	1.50E-07	0.0046	0.00758	1550	76	W2521
1.50E-06	3.00E-07	0.00758	0.011	1580	76	W2521
2.00E-06	6.00E-07	0.011	0.0147	1600	76	W2521
2.20E-06	5.00E-07	0.0147	0.0198	1650	76	W2521
3.30E-06	1.00E-06	0.0198	0.022	1700	76	W2521
9.00E-06	2.00E-06	0.022	0.0257	1750	76	W2521
1.20E-05	5.00E-06	0.0257	0.032	1800	76	W2521
7.00E-08	1.50E-08	0.0001	0.0002	635	480	W2526
5.00E-09	2.50E-09	0.0002	0.0005	475	480	W2526
1.00E-08	7.50E-09	0.0005	0.001	575	480	W2526
1.20E-08	1.00E-08	0.001	0.0013	645	480	W2526
3.00E-08	2.50E-08	0.0013	0.0021	725	480	W2526
2.00E-07	1.50E-07	0.0021	0.0028	975	480	W2526
8.00E-09	5.00E-09	0.0028	0.0032	505	480	W2526
1.50E-08	9.00E-09	0.0032	0.0036	595	480	W2526

Continuation of Table 1						
1.90E-08	1.50E-08	0.0036	0.004	695	480	W2526
3.50E-08	3.00E-08	0.004	0.0044	795	480	W2526
End of Table						

References

Amiguet, E., Van De Moortèle, B., Cordier, P., Hilairet, N., & Reynard, B. (2014). Deformation mechanisms and rheology of serpentines in experiments and in nature. *Journal of Geophysical Research: Solid Earth*, *119*(6), 4640–4655.

Burdette, E., & Hirth, G. (2020). Enhanced dehydration weakening of antigorite driven by slow shear heating: Insights from high-pressure experiments with a modified apparatus stiffness. *Journal of Geophysical Research: Solid Earth*, *125*(11), e2020JB020064.

Chernak, L. J., & Hirth, G. (2010). Deformation of antigorite serpentinite at high temperature and pressure [Journal Article]. *Earth and Planetary Science Letters*, *296*(1-2), 23-33. doi: 10.1016/j.epsl.2010.04.035

Escartin, J., Hirth, G., & Evans, B. (1997). Effects of serpentinization on the lithospheric strength and the style of normal faulting at slow-spreading ridges [Journal Article]. *Earth and Planetary Science Letters*, *151*(3-4), 181-189. doi: 10.1016/S0012-821x(97)81847-X

Hilairet, N., Reynard, B., Wang, Y., Daniel, I., Merkel, S., Nishiyama, N., & Petitgirard, S. (2007). High-pressure creep of serpentine, interseismic deformation, and initiation of subduction [Journal Article]. *Science*, *318*(5858), 1910-3. doi: 10.1126/science.1148494

Hirauchi, K.-i., Katayama, I., & Kouketsu, Y. (2020). Semi-brittle deformation of antigorite serpentinite under forearc mantle wedge conditions. *Journal of Structural Geology*, *140*, 104151.

Okazaki, K., & Hirth, G. (2016). Dehydration of lawsonite could directly trigger earthquakes in subducting oceanic crust [Journal Article]. *Nature*, *530*(7588), 81-4. doi: 10.1038/nature16501

Proctor, B., & Hirth, G. (2016). "ductile to brittle" transition in thermally stable antigorite gouge at mantle pressures [Journal Article]. *Journal of Geophysical Research: Solid Earth*, *121*(3), 1652-1663. doi: 10.1002/2015jb012710